Supporting information

Allying nitrogen-doped mesopore-dominated carbon electrode with anti-freezing $EMIBF_4$-GBL electrolyte for superior low-temperature supercapacitor

Jing Li,[†a] Yanan Zhou,[†a] Jiarui Tian,[b] Lele Peng,[e] Jie Deng,[a] Ning Wang,[c,d] Weizhong Qian,[b] and Wei Chu*[a]*

[a] *Department of Chemical Engineering, Sichuan University, Chengdu 610065, China*

[b] *Department of Chemical Engineering, Tsinghua University, Beijing 100084, China*

[c] *Advanced Membranes and Porous Materials Center, Physical Sciences and Engineering Division, King Abdullah University of Science and Technology, Thuwal 23955-6900, Saudi Arabia*

[d] *College of Environmental and Energy Engineering, Beijing University of Technology, Beijing 100124, China*

[e] *Department of chemistry and biochemistry, University of California, Los Angeles, Los Angeles 90095, U.S*

Corresponding Author

*Authors to whom correspondence should be addressed: Wei Chu (E-mail: chuwei1965@scu.edu.cn) and Ning Wang (E-mail: ning.wang.1@kaust.edu.sa)

† These authors contributed equally to this work.

Experimental section

Material synthesis: The N-doped mesoporous carbon (NMHC) electrode was synthesized by modifying our previous salt-templating strategy. To start, 1 g gelatin and 50 mg $Fe(NO_3)_2 \cdot 9H_2O$ was dissolved in 20 mL hot water at 80 ℃. The brown sol was formed. Subsequently, 0.75 g $NaNO_3$ was added. The sol was cooled at 4 ^oC for 12 h. After that, the as-obtained jell was immersed in liquid nitrogen for half a minute followed by freeze-drying in a lyophilizer at -80 ^oC, 1 Pa for 36 h. The as-obtained aerogel was annealed at 850 ^oC for 1 h in pure Ar gas with a flow rate of 300 mL/min and a heating rate of 5 ^oC/min. After that, the black aerogel was washed by the 2 M HCl and DI water to remove the template. Then, the sediment was flittered and dried at 60 ^oC for 24 h in an oven to get the powder. For the preparation of the binary electrolyte, $EMIBF_4$ (Chengjie Co. Ltd., Shanghai) and GBL (anhydrous, Aladdin) with different volume ratios ($EMIBF_4$/GBL = 1:0, 3:1, 1:1, 1:3, 0:1) were mixed in the glove box with the O_2 and moisture concentration lower than 0.1 ppm. In order to remove the moister, the commercial $EMIBF_4$ IL was firstly treated in the rotary evaporators with a rotation rate of 50 rpm at 70 ^oC and meanwhile vacuum pumped for 24 h prior to use.

Characterizations: X-ray diffraction (XRD) patterns were obtained on a diffractometer (Bruker D8 Advance) with Cu-Kα radiation at 40.0 kV and 120 mA in the range of 5-80 ^{o} with the scanning rate of 10 ^{o}/min. The low-temperature test was conducted by pre-cooling the electrolyte and then immediately transferring to the testing chamber. Raman spectra were recorded on Raman spectrophotometer (Horiba Jobin Yvon LabRAM HR800) with He-Ne laser excitation at 633 nm. Prior to the Raman tests, the electrolyte was sealed in a capillary tube (1 mm by diameter) to prevent the contamination from the air. The ^1H nuclear magnetic resonance (NMR) was conducted in a JNM-ECA600 NMR spectrometer. The electrolyte was sealed by the capillary tube to rule out

the intervention of the interaction with the solvent. During the test, the electrolyte was separated from the reference solvent (deuterium oxide, D_2O). The N_2 adsorption/desorption isotherm was recorded by an Autosorb-IQ2-MP-C system to get the specific surface area calculated by the multipoint Brunauer-Emmett-Teller (BET) method, and the pore-size distribution based on Quenched Solid Density Function Theory (QSDFT) model using the adsorption branch. The morphology of NMHC was characterized by a scanning electron microscope (SEM, JSM 7401F, JEOL Ltd., Tokyo, Japan) operated at 3.0 kV, and a transmission electron microscope (TEM, JEM 2010, JEOL Ltd., Tokyo, Japan) operated at 120.0 kV. X-ray photoelectron spectroscopy (XPS) measurements conducted on Escalab 250xi.

Electrochemical measurements: The electrode ink was prepared by mixing active materials, acetylene black, PVDF binder with a weight ratio of 1: 1: 1 in NMP solvent. The carbon-coated aluminum foil was used as the current collector. The specific amount of the electrode ink was dropped onto the foil (1.1 cm in diameter) and followed by the vacuum drying, obtaining an electrode with a mass loading of 1 mg cm^{-2}. The neat $EMIBF_4$ ILs and the binary $EMIBF_4$-GBL mixture were served as the electrolyte. Whatman membrane (680 μm in thickness), made from glass microfibre (type: GF/D1823-047) was used as the separator. Symmetric two-electrode 2025-type coin cell was assembled in the pure Ar gloves with concentrations of both oxygen and moisture lower than 0.1 ppm.

The as-assembled coin SCs were aged in a chamber (Cincinati Sub-Zero, America) to stabilize at a specific temperature (-50 ^oC – 20 ^oC) and the capacitance performance including cyclic voltammetry (CV), galvanostatic charge-discharge (GCD) and electrochemical impedance spectroscopy (EIS) were conducted on an electrochemical workstation (EC Lab, France). The ion conductivity (σ) of the neat $EMIBF_4$ and $EMIBF_4$-GBL binary electrolyte at 20 ^oC was measured

by the conductivity meter firstly. The ion conductivity at other temperatures can be calculated from the equation:

$\sigma = k/R\text{s}$,

where k is a constant, and σ is inversely proportional to the solution resistant (Rs) in EIS spectra.

The charge (Q) stored on the electrode in charge or discharge process was calculated from the CV curve based on the equation:

$$S = \oint idU = \oint ivdt = v\oint idt = 2vQ$$

So the charge $Q = S/2v$, where v is the scan rate, S is the integral area of CV curve.

The specific capacitance ($C_{\text{electrode}}$, F g^{-1}) based on each electrode was calculated by using the formula:

$C_{\text{electrode}} = 4I\Delta t/mV$,

where I, Δt, m, and V are the constant current (mA), discharge time (s), the total mass of both carbon electrode (mg), and the voltage window (V).

The energy density (E, Wh kg^{-1}) was calculated based on the equation:

$E = C_{\text{cell}}\ V^2/7.2 = C_{\text{electrode}}V^2/28.8$

The power density (P, W kg^{-1}) was obtained according to the formula:

$P = E/\Delta t$

Computation section: The calculations of the density functional theory (DFT) with long-range dispersion correction (DFT-D) were carried out using $Dmol^3$ code within the Materials Studio.

The generalized gradient approximation (GGA) with the Perdew, Burke, and Ernzerhof (PBE) was used to describe the electron exchange and correlation interactions. All electron calculation was employed as the core treatment with the double numerical plus polarization (DNP) was used as the basis set. The thermal smearing value was chosen at 0.005 Hartree and spin unrestricted was selected. The convergence criterions in total energy, maximum force, and maximum displacement were set at 1×10^{-5} Hartree, 2×10^{-3} Hartree/Å, and 5×10^{-3} Å, respectively.

The binding energy (E_b) was calculated according to the following equation:

$$E_b = E_{A+B} - E_A - E_B$$

Here, E_{A+B}, $E_{A,}$ and E_B refer to the total energy of A and B complex, isolated A and B, respectively.

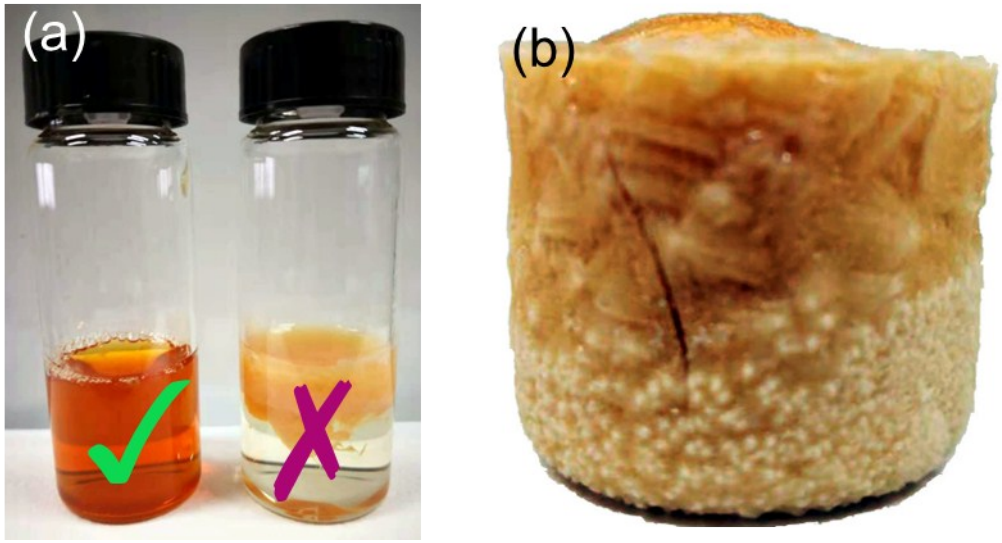

Fig. S1. (a) The adding order of two salts ($NaNO_3$ and $Fe(NO_3)_3$) led to different results: left) uniform sol by adding $Fe(NO_3)_3$ firstly and then $NaNO_3$, right) precipitation by adding $NaNO_3$ firstly and then $Fe(NO_3)_3$. (b) The photograph of the aerogel foam via dual-slat-template method.

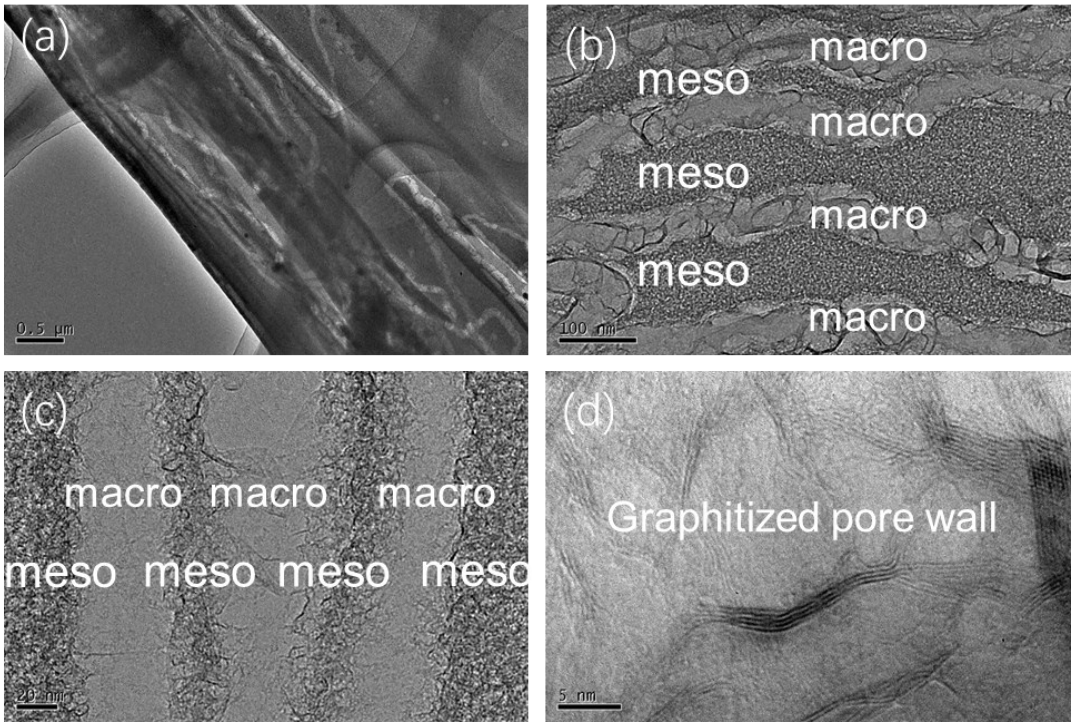

Fig. S2. Several randomly selected TEM images of NMHC electrode, showing that (a) the macropore channel crosses the whole body of the material, (b, c) unique sandwich-type meso-macro-mesoporous structure of NMHC, and (d) the graphitized pore wall of NMHC.

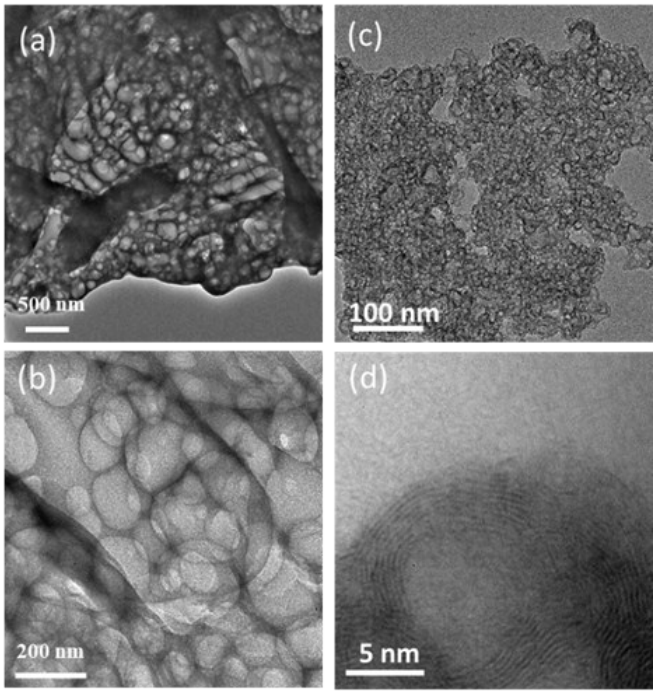

Fig. S3. TEM images of counterpart samples synthesized by one kind of salt-template. (a, b) $NaNO_3$ template, and (c, d) $Fe(NO_3)_3$ template.

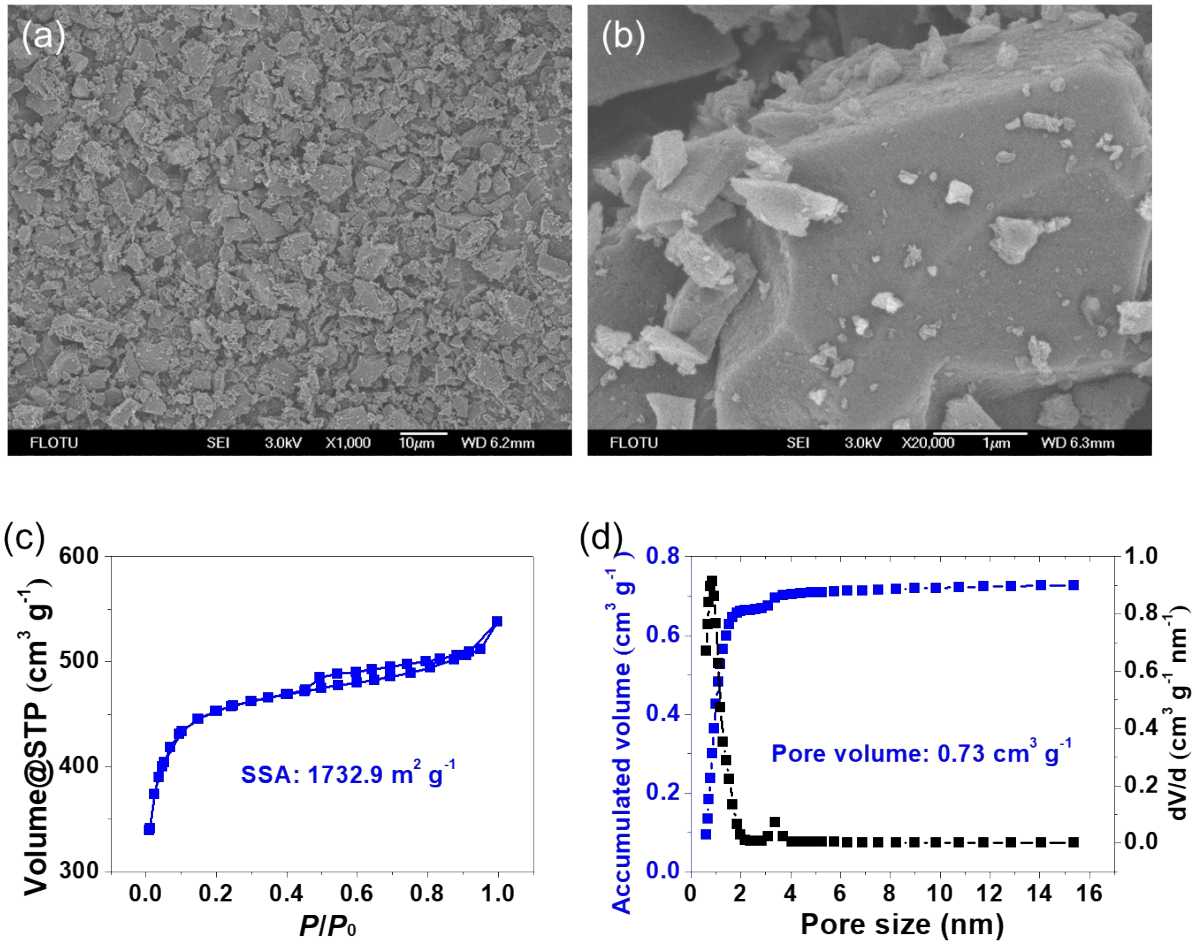

1

2 **Fig. S4.** (a, b) SEM images of commercial YP50 electrode, and (c, d) specific surface area and

3 pore volume and pore size distribution of YP50.

4

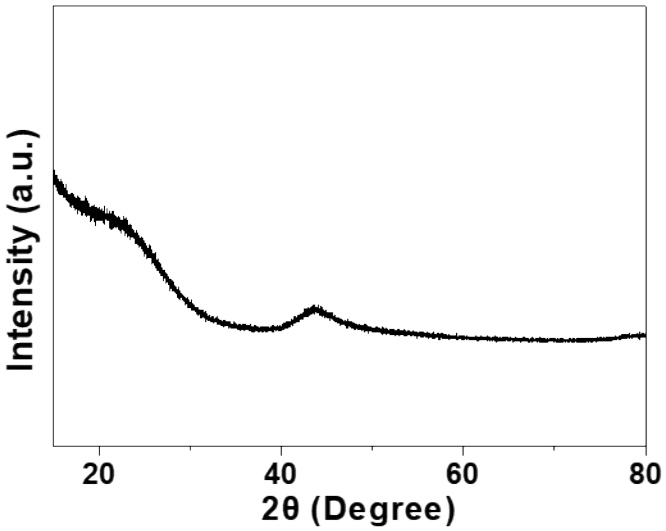

1

2 **Fig. S5.** XRD result of YP50.

3

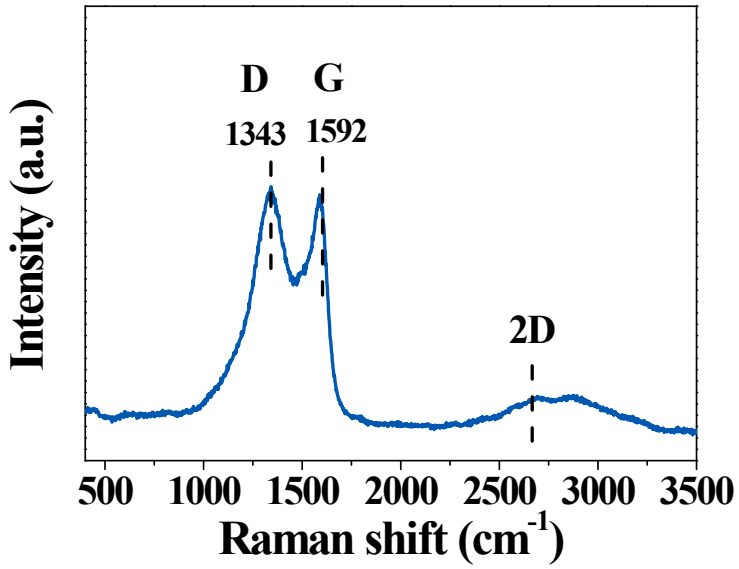

Fig. S6. Raman spectrum of NMHC.

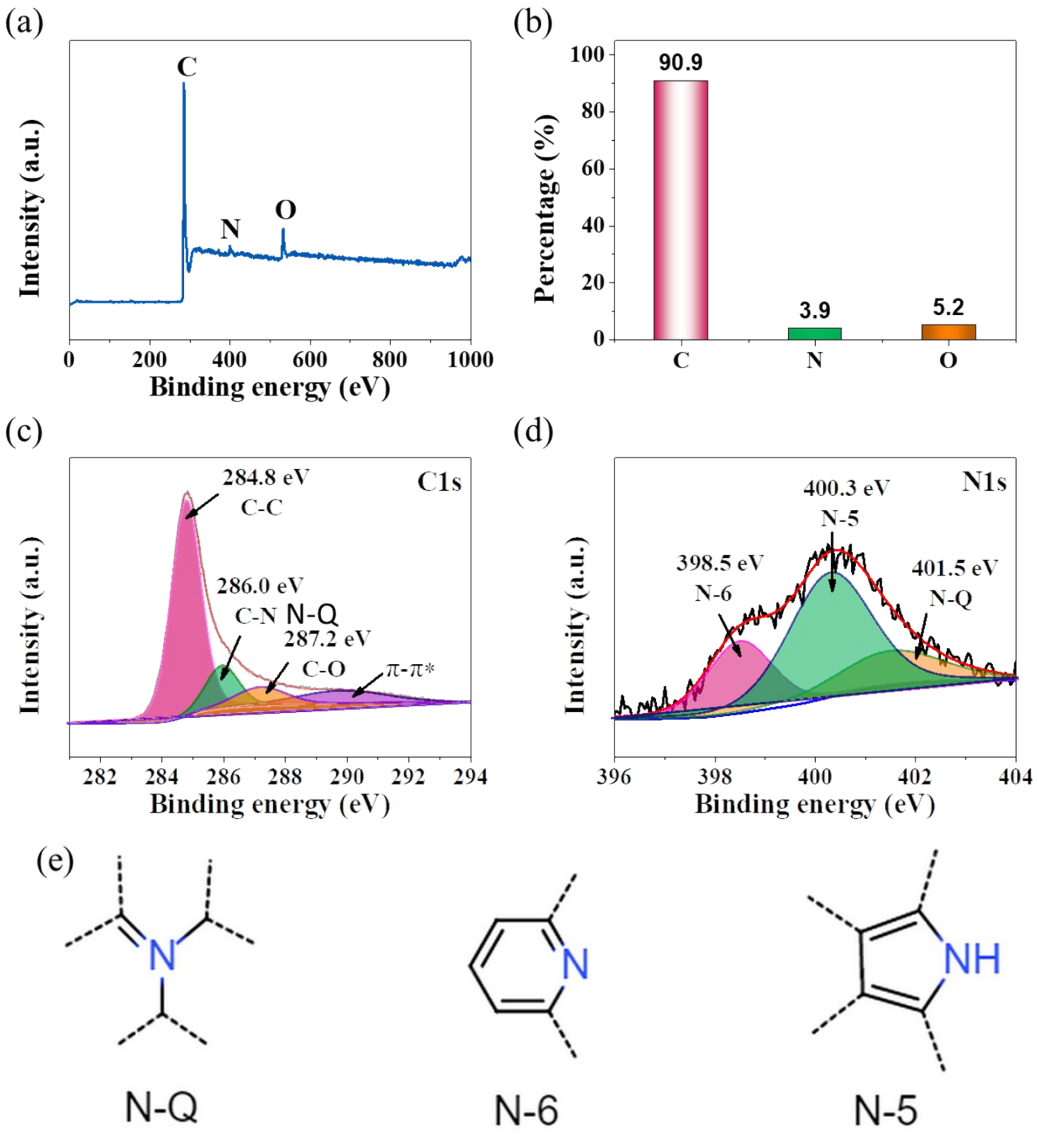

1

2 **Fig. S7.** (a) XPS survey spectrum of NMHC. (b) The element content of C, N, O. (c) C1s
3 spectrum, and (d) N1s spectrum of NMHC electrode. (e) The assignment of N-Q, N-6, and N-5.

4

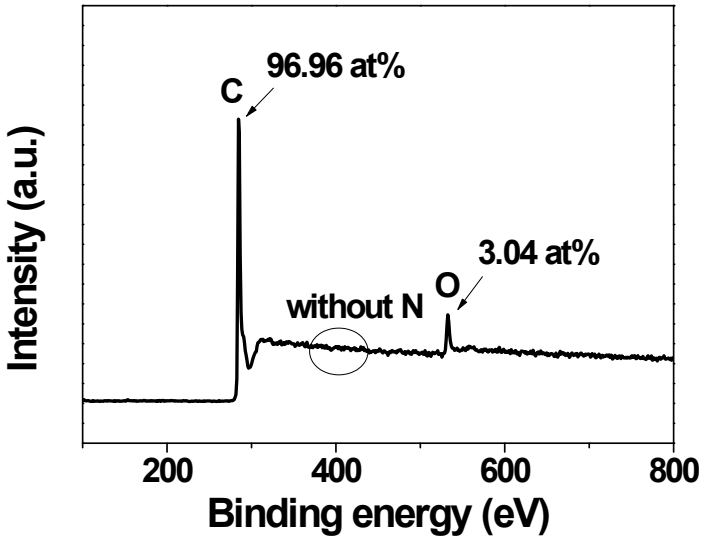

Fig. S8. XPS result of YP50.

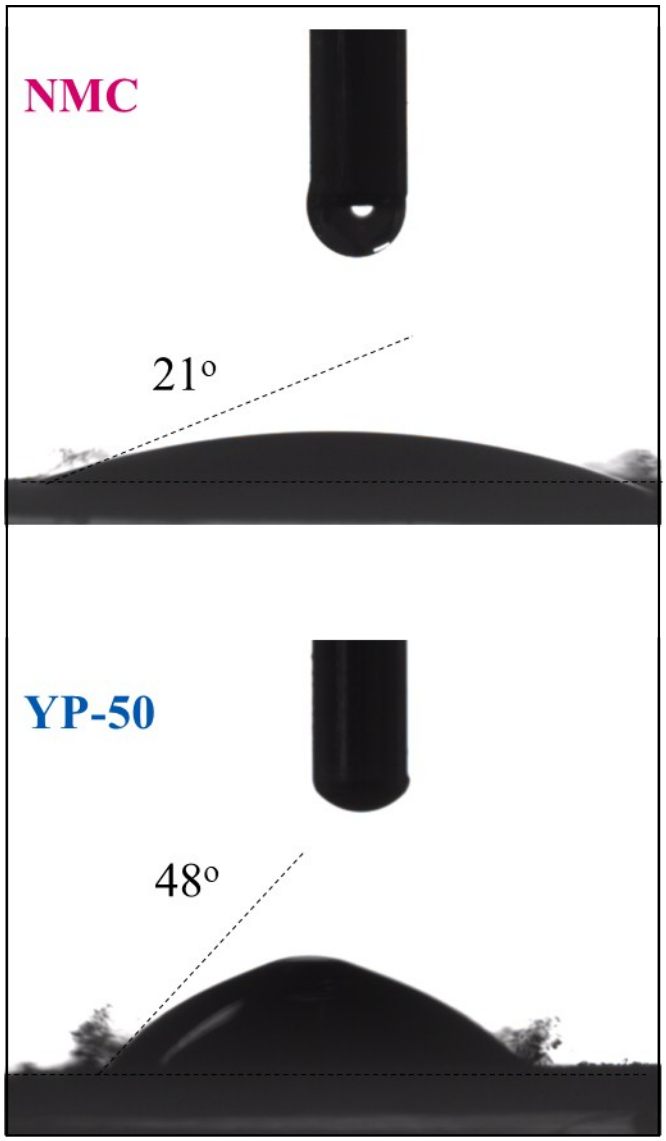

Fig. S9. The contact angle test of NMHC and YP50 electrodes to measure their wetting ability to $EMIBF_4$-GBL electrolyte.

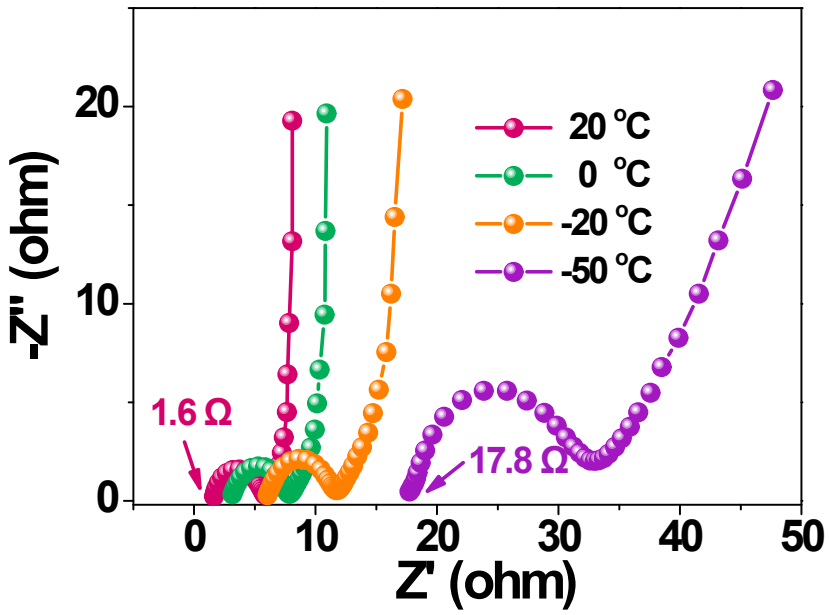

Fig. S10. The EIS spectra of $EMIBF_4$-GBL electrolyte under different temperatures.

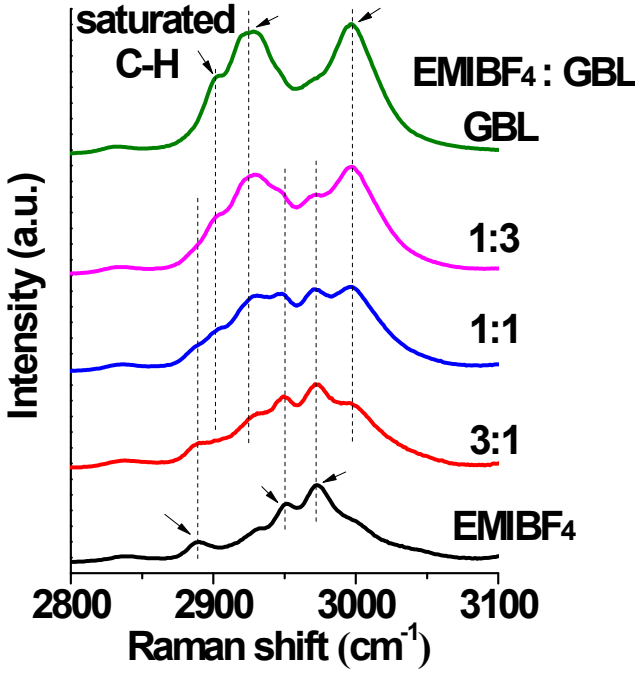

Fig. S11. Raman spectra of the saturated C-H bonds in $EMIBF_4$ (C-6H, C-7H, and C-8H), and in GBL ($C\text{-}2H_{GBL}$, $C\text{-}3H_{GBL}$, and $C\text{-}4H_{GBL}$).

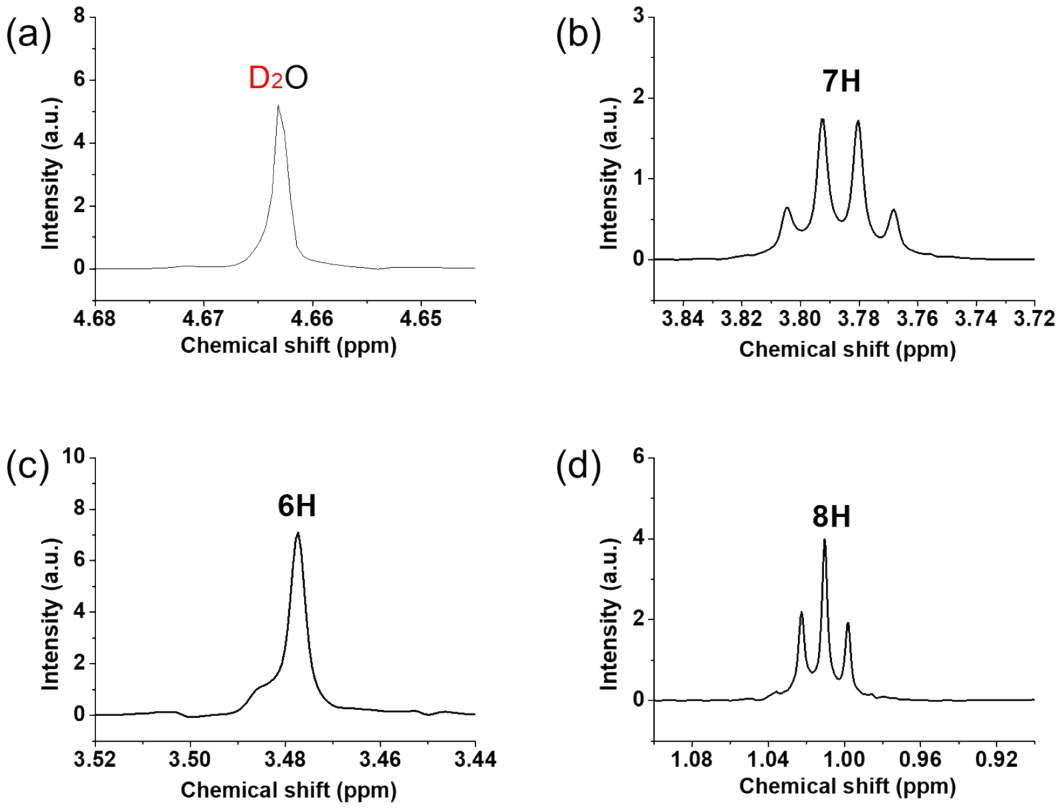

Fig. S12. The chemical shift of D_2O, 7H, 6H, and 8H of neat $EMIBF_4$.

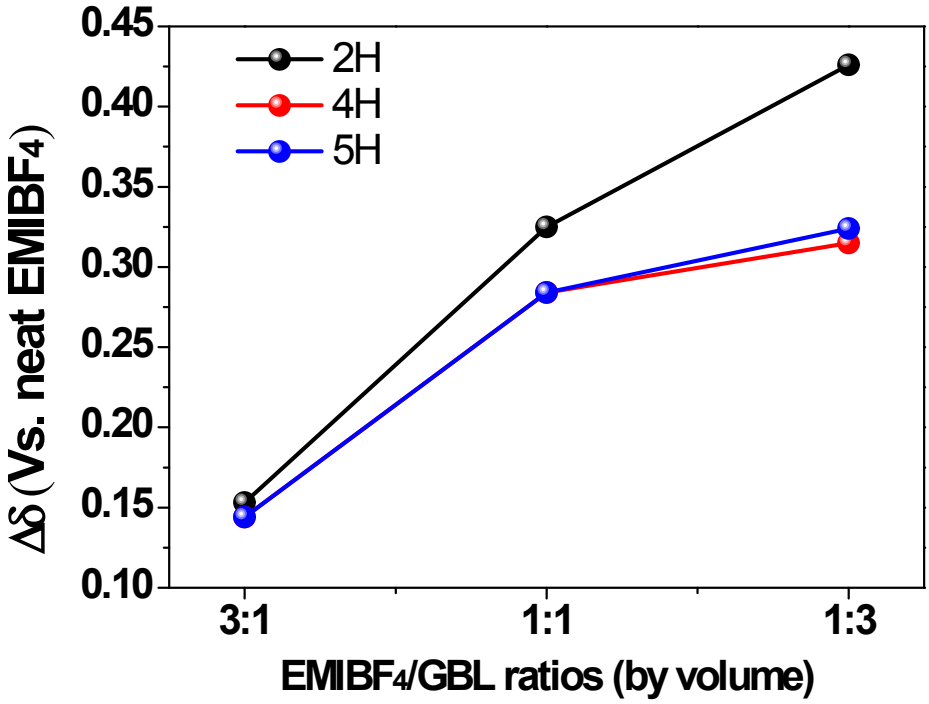

Fig. S13. The increments of chemical shifts of 2H, 4H, 5H in different $EMIBF_4$/GBL ratios versus neat $EMIBF_4$ IL.

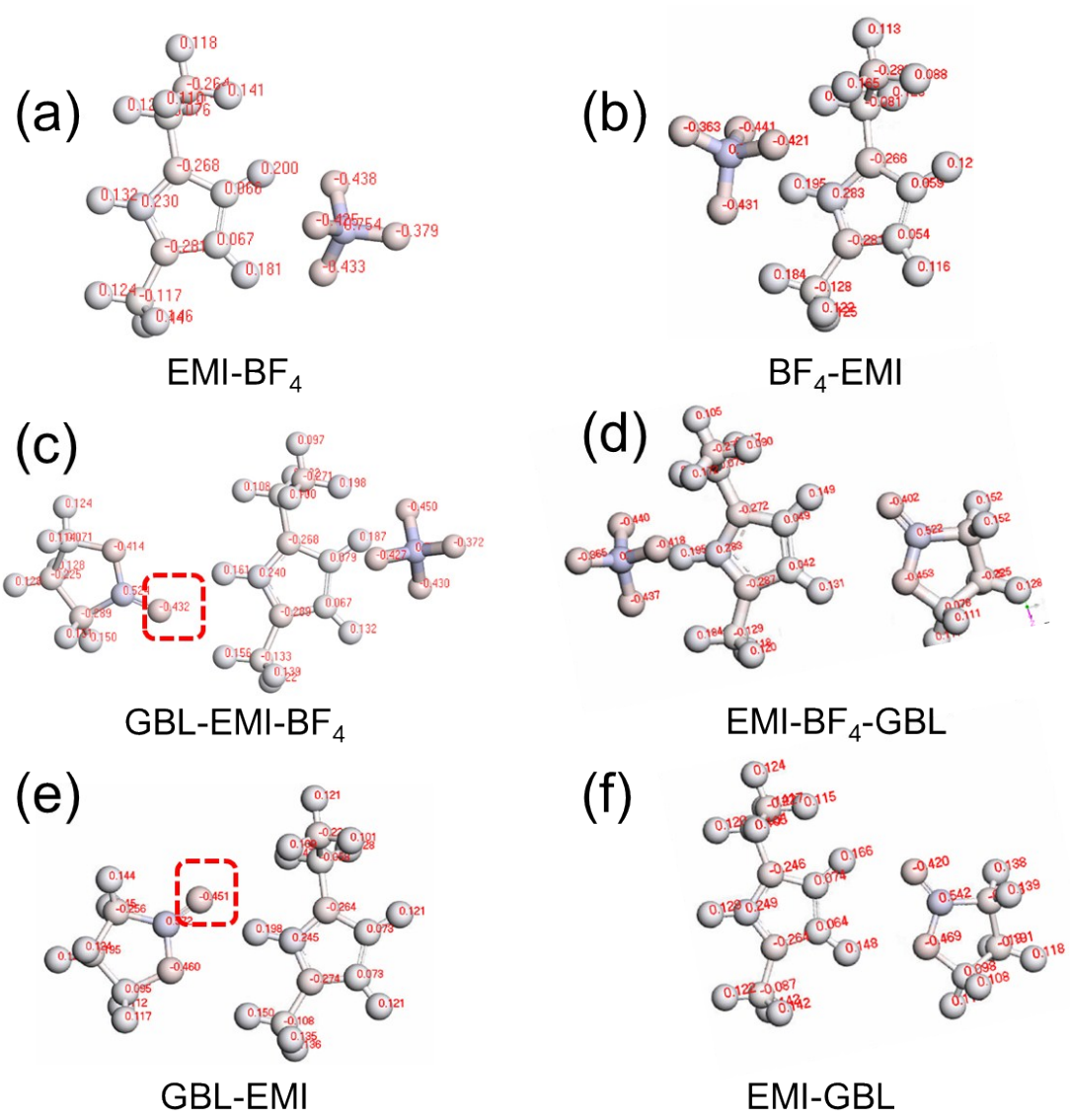

Fig. S14. The electrostatic potential graphs of a) EMI-BF_4, b) BF_4-EMI, c) GBL-EMI-BF_4, d) BF_4-EMI-GBL, e) GBL-EMI, and f) BF_4-GBL.

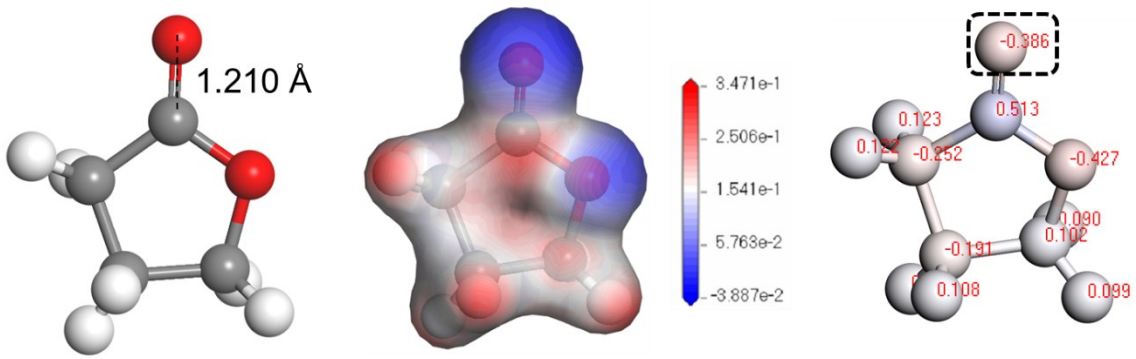

Fig. S15. The electrostatic potential graphs of GBL.

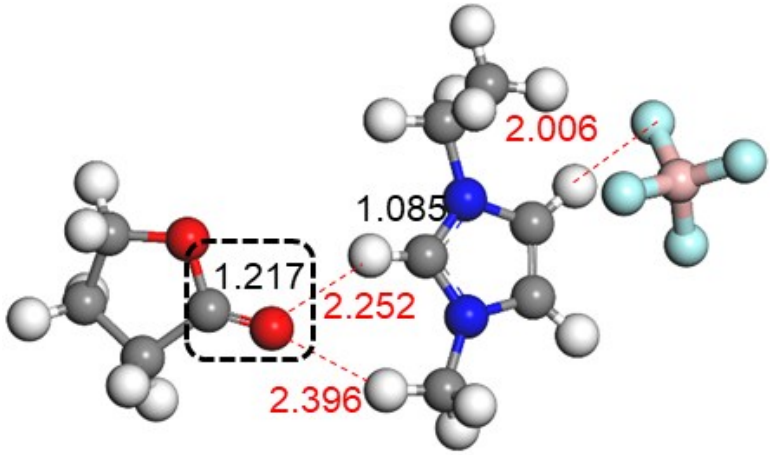

Fig. S16. The C=O bond was starched in BF_4-GBL-EMI compared with that in bare GBL.

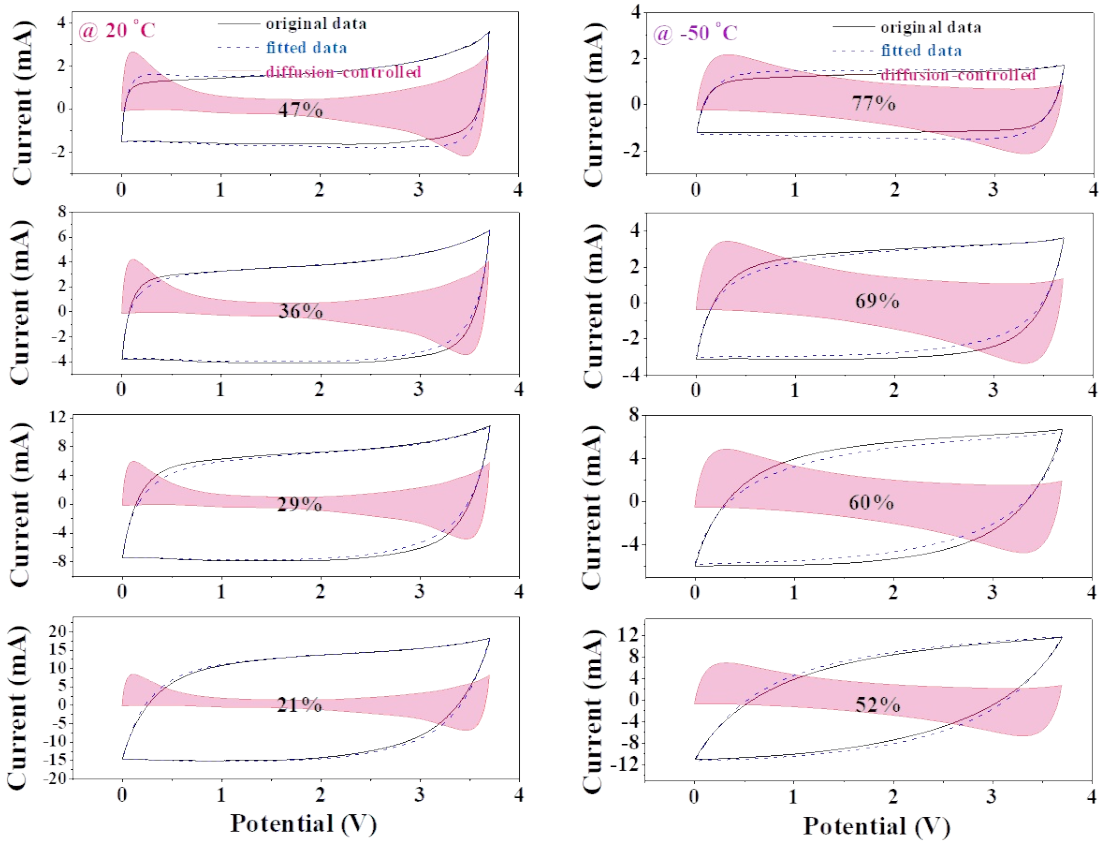

Fig. S17. Fitting data of diffusion-controlled current of CV curves of NMHC electrode at the scan rate of 20, 50, 100, 200 mV s^{-1} (from top to bottom) and the temperature of 20 and -50 °C, respectively.

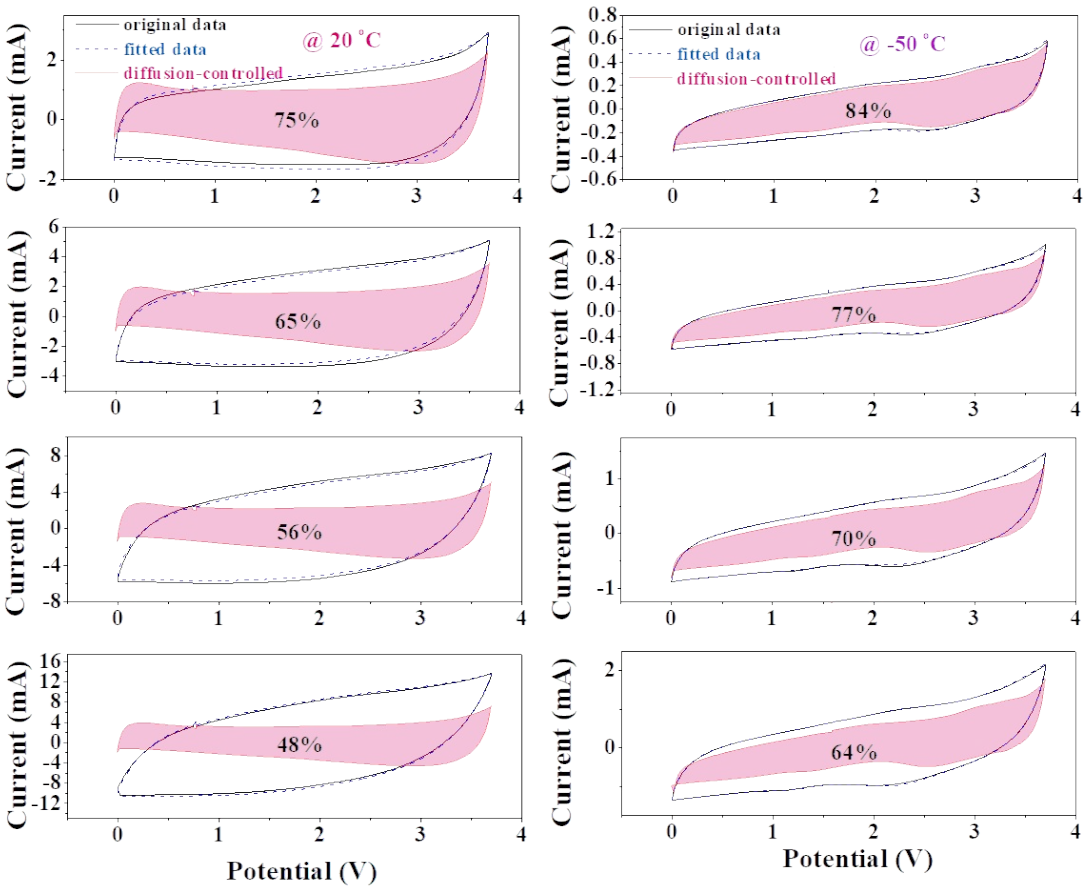

Fig. S18. Fitting data of diffusion-controlled current of CV curves of YP50 electrode at the scan rate of 20, 50, 100, 200 mV s^{-1} (from top to bottom) and the temperature of 20 and -50 °C, respectively.

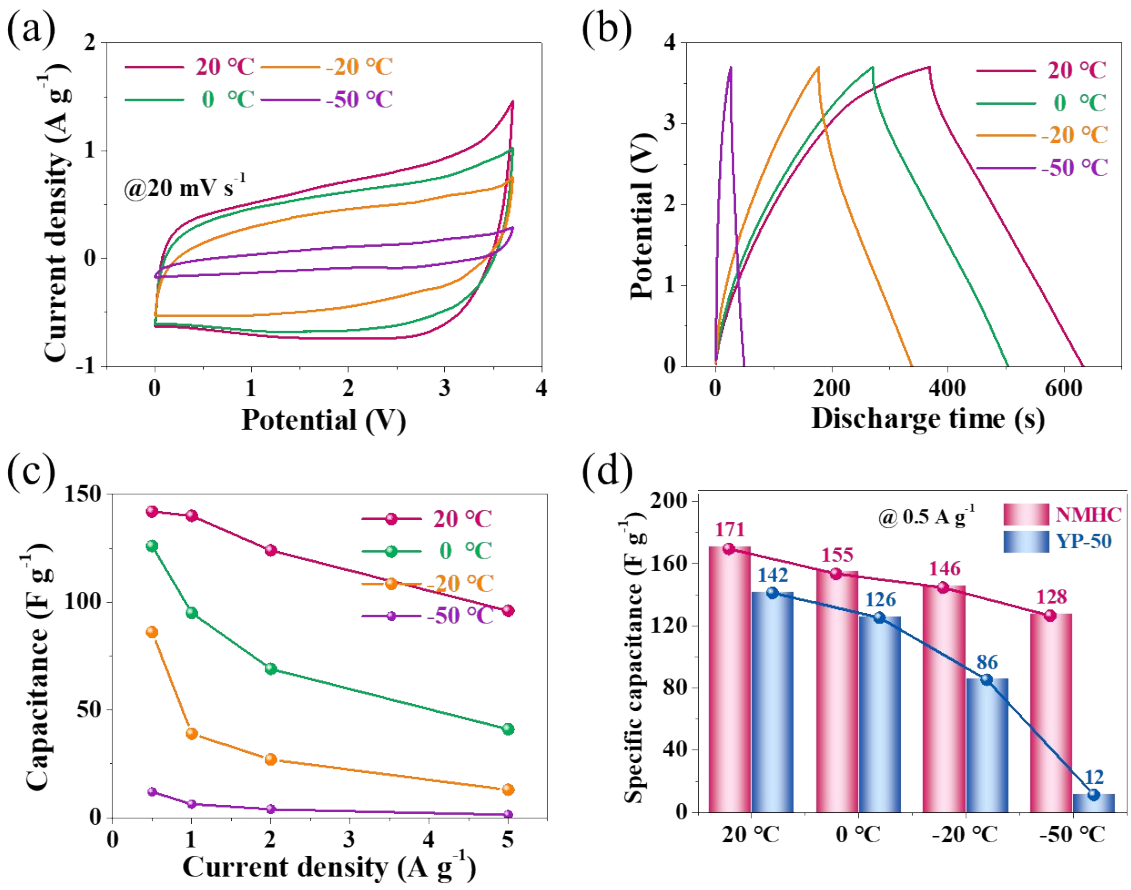

Fig. S19. (a) CV, (b) CD, and (c) rate capability of YP50 electrode. (d) Comparison of specific capacitance between NMHC and YP50 from 20 to -50 °C.

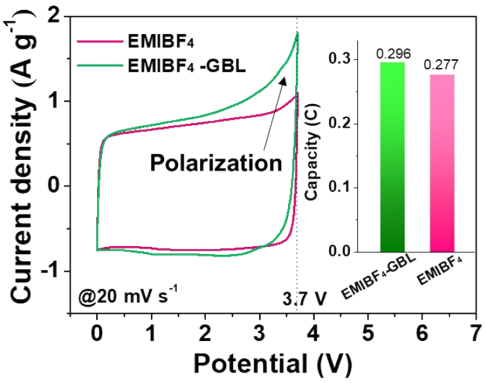

Fig. S20. CV curves using $EMIBF_4$ and $EMIBF_4$-GBL as electrolyte at 20 mV s^{-1} and 20 ^oC, and the calculated capacities from the CV curves.

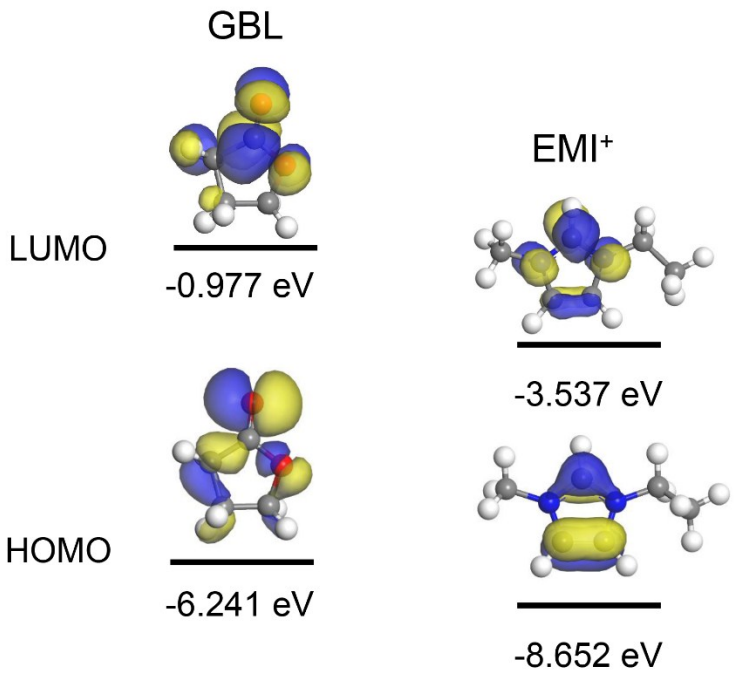

Fig. S21. HOMO and LUMO level of GBL and EMI^+.

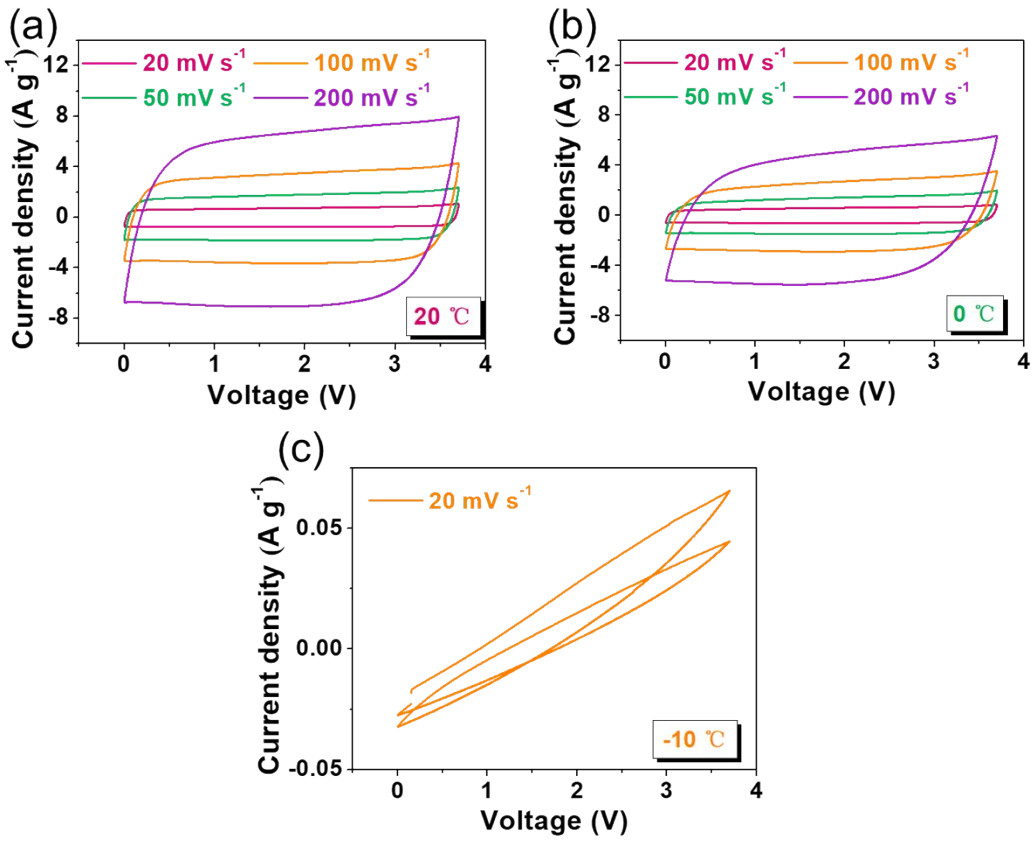

Fig. S22. CV curves of NMHC electrode using neat $EMIBF_4$ as the electrolyte under different temperatures and scan rates.

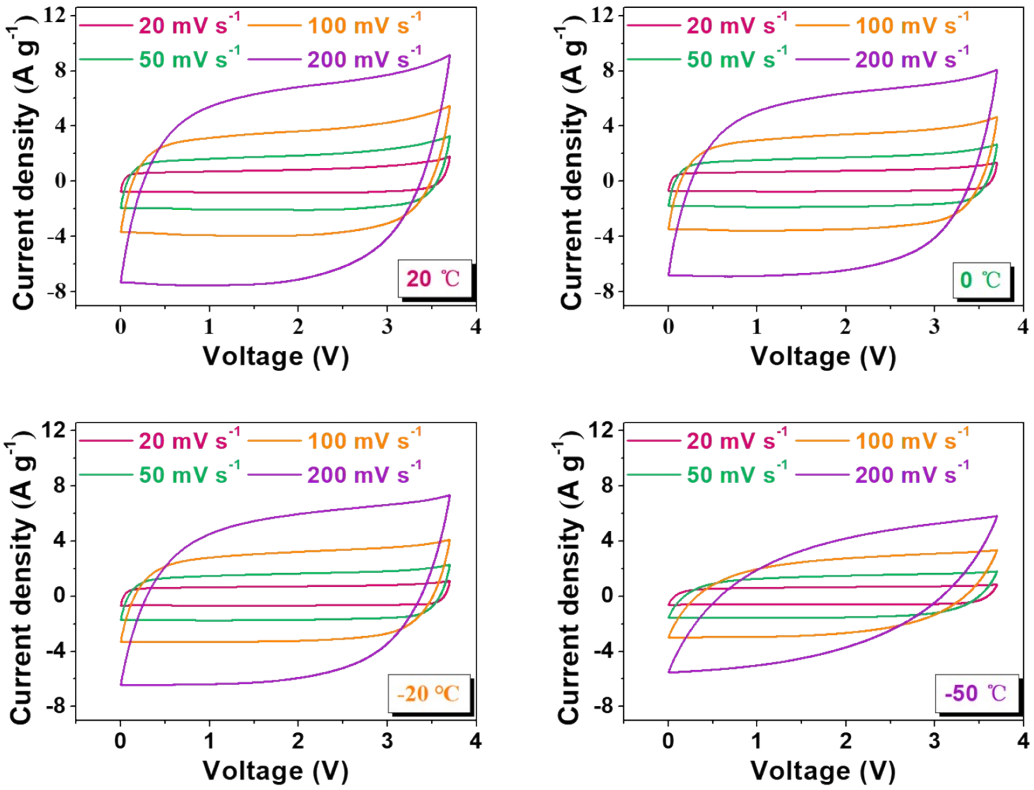

Fig. S23. CV curves of NMHC electrode in binary $EMIBF_4$-GBL electrolyte under different temperatures and scan rates.

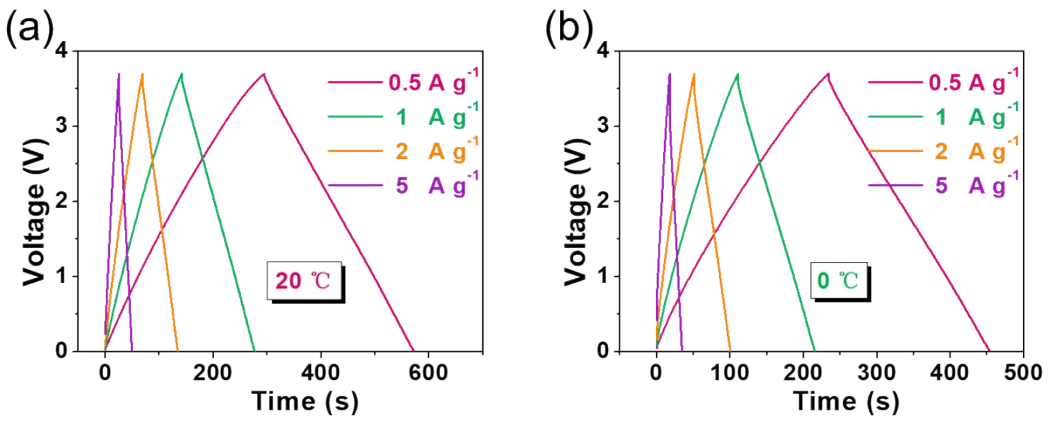

Fig. S24. CD curves of NMHC electrode in neat $EMIBF_4$ electrolyte under different temperatures and current densities.

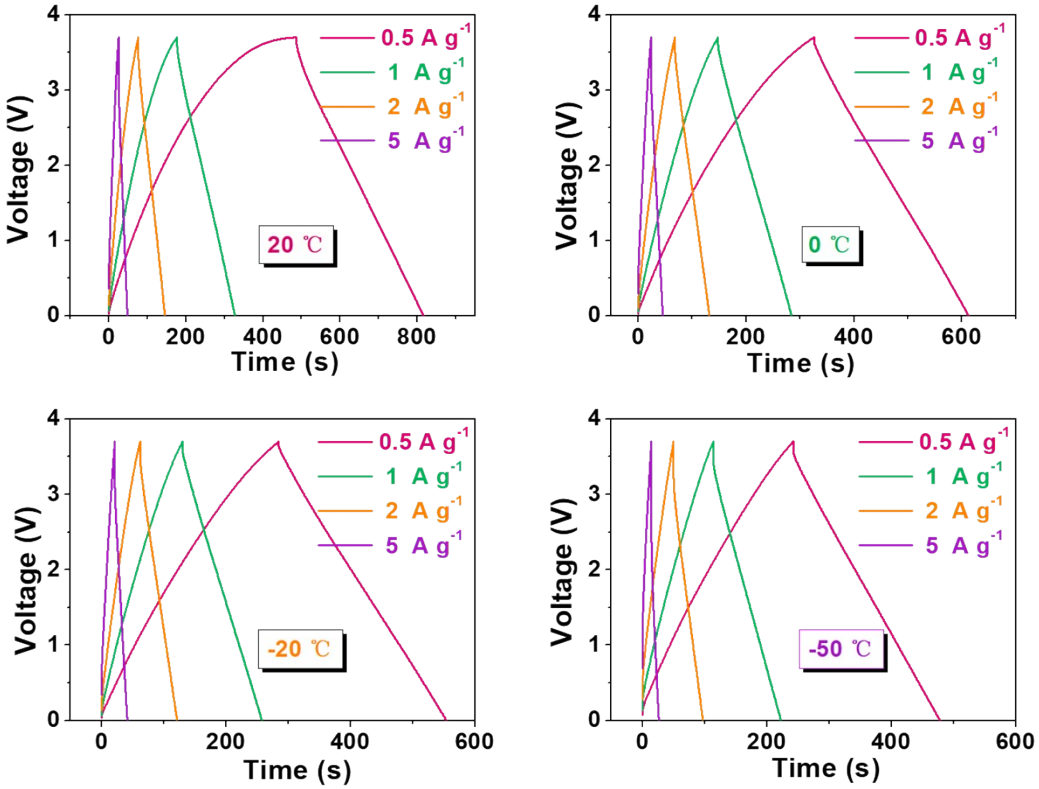

Fig. S25. CD curves of NMHC electrode in binary $EMIBF_4$-GBL electrolyte under different temperatures and current densities.

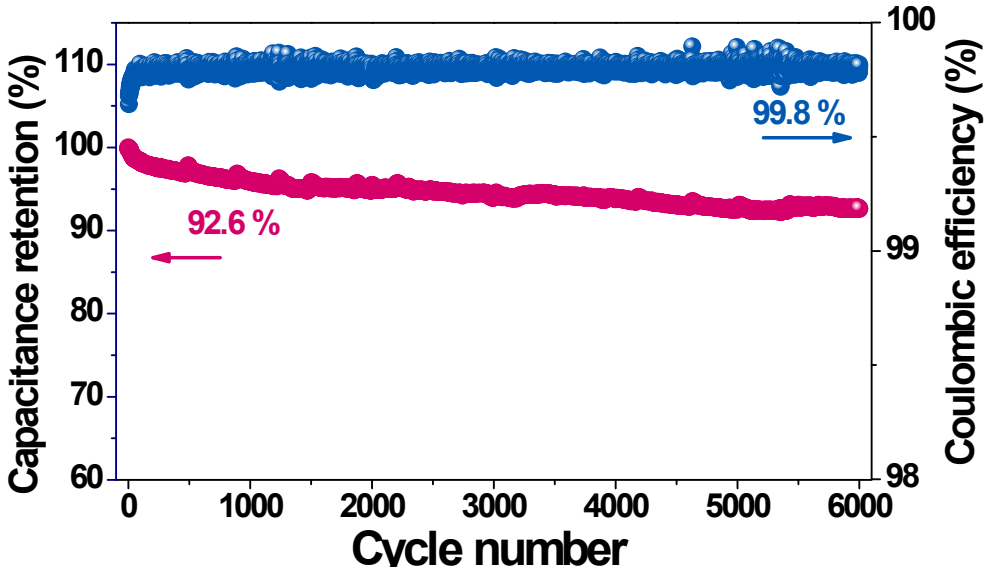

Fig. S26. The cycling performance of NMHC electrode using $EMIBF_4$-GBL under -50 °C at 5 A g^{-1}.

Table S1. The physical properties of four kinds of solvent in low-temperature electrolyte. GBL is more suitable to sustain a high voltage [2-5].

Solvent		molecular weight (g/mol)	Melting point (M.P., °C)	Boling point (B.P., °C)	Voltage window (V)	HOMO (eV)	LUMO (eV)
Ethyl acetate [2]	(EA)	88.11	-84	77	2.1	-6.188	0.830
1,3-dioxolane [3]	(DOL)	74.08	-95	78	2.5	-5.803	1.409
Acetonitrile [4]	(ACN)	41.05	-45	81	2.7	-7.938	-0.233
γ-butyrolactone [5]	(GBL)	86.1	-43	206	3.7	-6.241	-0.977

Table S2. ^{1}H NMR chemical shifts of H atoms in EMI^{+}.

$EMIBF_4$:GBL	2H	4H	5H	7H	6H	8H
1:0	8.176	7.122	7.050	3.793	3.477	1.010
3:1	8.329	7.266	7.194	3.933	3.606	1.155
1:1	8.501	7.406	7.334	4.064	3.738	1.300
1:3	8.602	7.437	7.374	4.126	3.797	1.380

Table S3. ^{1}H NMR chemical shifts of H atoms in GBL.

$EMIBF_4$:GBL	$2H_{GBL}$	$3H_{GBL}$	$4H_{GBL}$
3:1	2.142	1.887	3.985
1:1	2.283	2.030	4.140
1:3	2.400	2.126	4.258
0:1	2.448	2.179	4.308

Table S4. The length of H-bonds and C-H bonds.

Configurations	$r_{H\text{-}F}$ (Å)	$r_{H\text{-}O}$ (Å)	$r_{H\text{-}C}$ (Å)
$EMI\text{-}BF_4$	4H···F (2.128) 5H···F (1.982)	-	C-4H (1.087) C-5H (1.091)
BF_4-EMI	2H···F (2.027)	-	C-2H (1.086)
GBL-EMI-BF_4	5H···F (2.006)	2H···O (2.252)	C-2H (1.085)
BF_4-EMI-GBL	2H···F (2.604)	5H···O (2.369)	C-2H (1.084)
GBL-EMI	-	2H···O (1.919)	C-2H (1.096)
EMI-GBL	-	5H···O (2.196)	C-4H (1.085) C-5H (1.084)

Table S5. The summarize of solution resistance (*R*s) and charge transfer resistance (*R*ct) of NMHC and YP50 electrode under different temperatures.

Temperature (℃)	YP-50		NMHC	
	*R*s (Ω)	*R*ct (Ω)	*R*s (Ω)	*R*ct (Ω)
20	2.0	17.2	1.6	4.6
0	2.8	38.8	3.2	5.2
-20	4.9	46.5	6.0	6.0
-50	19.5	74.3	17.7	15.1

Table S6. The performance comparison of ILs-based high-voltage EDLCs under various working temperatures.

Materials	**Electrolyte**	**m (mg/cm^2)**	**Current collector**	***T*** **(^{o}C)**	***V*** **(V)**	***C*** **(F/g)**	***E*** **(Wh/kg)**	***P*** **(kW/kg)**	**Ref.**
N-doped mesoporous carbon	$EMIBF_4$	1	Ni foam	25	4	169 (0.5 A/g)	92 39	1 200	(1)
	$EMIBF_4$-GBL	**1**	**Carbon coated Al foil**	**-50** **20**	**3.7** **3.7**	**128** **171** **(0.5 A/g)**	**61** **81**	**0.925** **0.925**	**This work**
Graphene nanofiber	$EMIBF_4$	-	Ni form	25	4	193 (0.5 A/g)	105	1	(6)
	$EMIBF_4$-GBL	1.6	Al foil	**-70**	3.7	131 (0.2 A/g)	61	0.37	(5)
CNT buckypaper	$PYR_{14}TFSI$-CNT	-	Free standing	25	5	-	90 15	0.06 2	(7)
Graphene	$EMIBF_4$ EMITFSI	0.5	Al foil	25	4	192 244 (5 A/g)	106 136	-	(8)
Honey graphene	$EMIBF_4$/AN	10	Free standing	25	3.5	298 (1 A/g)	127	1.75	(9)
		10 (150 μm)				316 (1 A/g)	134	1.75	(10)
CNT arrays	$PIP_{13}FSI$-$PYR_{14}FSI$	-	Al foil	**-50** 100	3.5 2.8	-	-	-	(11)
Activated graphene		1.5	Pt foil	**-50** 20 80	3 3.5 2.9	100 160 180	31 68 53	-	(12)

References:

(1) Li, J.; Wang, N.; Tian, J.; Qian, W.; Chu, W., *Adv. Funct. Mater.* **2018,** *28* (51), 1806153.

(2) Dong, X.; Guo, Z.; Guo, Z.; Wang, Y.; Xia, Y., *Joule* **2018,** *2* (5), 902-913.

(3) Xu, J.; Yuan, N.; Razal, J. M.; Zheng, Y.; Zhou, X.; Ding, J.; Cho, K.; Ge, S.; Zhang, R.; Gogotsi, Y.; Baughman, R. H., *Energy Storage Mater.* **2019,** *22*, 323-329.

(4) Iwama, E.; Taberna, P. L.; Azais, P.; Brégeon, L.; Simon, P., *J. Power Sources* **2012,** *219*, 235-239.

(5) Tian, J.; Cui, C.; Xie, Q.; Qian, W.; Xue, C.; Miao, Y.; Jin, Y.; Zhang, G.; Guo, B., *J. Mater. Chem. A* **2018,** *6* (8), 3593-3601.

(6) Cui, C.; Qian, W.; Yu, Y.; Kong, C.; Yu, B.; Xiang, L.; Wei, F., *J. Am. Chem. Soc.* **2014,** *136* (6), 2256-2259.

(7) Kong, C.; Qian, W.; Zheng, C.; Fei, W., *J. Mater. Chem. A* **2015,** *3* (31), 15858-15862.

(8) Li, C.; Zhang, X.; Wang, K.; Sun, X.; Liu, G.; Li, J.; Tian, H.; Li, J.; Ma, Y., *Adv. Mater.* **2017,** *29* (7), 1604690.

(9) Pan, Z.; Zhi, H.; Qiu, Y.; Yang, J.; Xing, L.; Zhang, Q.; Ding, X.; Wang, X.; Xu, G.; Yuan, H.; Chen, M.; Li, W.; Yao, Y.; Motta, N.; Liu, M.; Zhang, Y., *Nano Energy* **2018,** *46*, 266-276.

(10) Xu, Y.; Lin, Z.; Zhong, X.; Huang, X.; Weiss, N. O.; Huang, Y.; Duan, X., *Nat. Commun.***2014,** *5* (1), 4554.

(11) Lin, R.; Taberna, P.-L.; Fantini, S.; Presser, V.; Pérez, C. R.; Malbosc, F.; Rupesinghe, N. L.; Teo, K. B. K.; Gogotsi, Y.; Simon, P., *J. Phys. Chem. Lett.* **2011,** *2* (19), 2396-2401.

(12) Tsai, W.-Y.; Lin, R.; Murali, S.; Li Zhang, L.; McDonough, J. K.; Ruoff, R. S.; Taberna, P.-L.; Gogotsi, Y.; Simon, P., *Nano Energy* **2013,** *2* (3), 403-411.